Numerical and Experimental Investigation of Ultrafine Particle Transport and Deposition in a Human Upper Airway Model

F. Krause[1], A. Wenk[2], W. Möller[2], S. Verbanck[3], C. Lacor[4], and W. G. Kreyling[2]

[1] Vrije Universiteit Brussel, Department of Mechanical Engineering, Fluid Dynamics and Thermodynamics Research Group
Pleinlaan 2, 1050 Brussel, Belgium, fkrause@vub.ac.be

[2] Helmholtz Zentrum München, German Research Center for Environmental Health, Institute of Lung Biology and Disease
Ingolstaedter Landstrasse 1, 85764 Neuherberg, Germany, {alexander.wenk, moeller, kreyling}@helmholtz-muenchen.de

[3] University Hospital UZ Brussel, Respiratory Division
Laarbeeklaan 101, 1090 Brussel, Belgium, sylvia.verbanck@uzbrussel.be

[4] Vrije Universiteit Brussel, Department of Mechanical Engineering, Fluid Dynamics and Thermodynamics Research Group
Pleinlaan 2, 1050 Brussel, Belgium, chris.lacor@vub.ac.be

Abstract

The majority of the published numerical studies on the deposition of ultrafine particles in the human upper airways lack the validation of the predicted flow field and particle deposition. Thus, this study aims at validating the numerically predicted laminar-turbulent flow field and subsequent deposition of ultrafine particles in a realisitic model of the human upper airways by means of experimental in vitro measurements. The simulated flow field is compared to existing particle image velocimetry measurements and the total deposition results are compared to experimental deposition measurements of ultrafine carbon particles in a cast of the same upper airway model.

Monodisperse ultrafine carbon particles of different thermodynamic diameter ranging from $d_p = 14.5nm$ to $d_p = 52nm$ are generated by spark ignition and their deposition in a silicone cast of the upper airway model is measured for three physiologically relevant steady inhalation flow rates $Q = 10, 20$ and $30\frac{l}{min}$. Computations of the laminar-turbulent flow field are carried out using an open-source steady-state solver for incompressible, turbulent flows in conjunction with the k-ω SST RANS turbulence model. For the simulation of the particle motion and the subsequent particle deposition, the Eulerian mass transport model is employed.

Both simulations and experiments show that total particle deposition fraction increases with decreasing flow rate and decreasing particle diameter. Furthermore, simulations as well as experiments are in satisfactory quantitative agreement with previous numerical and experimental data. A direct comparison in the range of flow rate ($Q > 10\frac{l}{min}$) and particle size ($d_p > 14.5nm$) that are achieved experimentally, reveals that the simulated total deposition is approximately half the experimental value. However, this discrepancy needs to be considered in the light of the very low deposition efficiencies in this flow and size range (with all experimental deposition fractions less than 5%).

Finally, the simulations also serve to identify local deposition hot-spots by contours of the so-called deposition enhancement factor. Although the local deposition results cannot be validated quantitatively, they show that the deposition pattern is more discrete as particle size decrease. This observation is in line with previous studies.

Keywords: human upper airway model, ultrafine particle deposition, Reynolds-averaged Navier-Stokes equations, Eulerian mass transport model

Introduction

During the last number of decades, the inhalation exposure to airborne nano-sized particles has increased significantly because of its widespread use and production in diverse sectors in science, technology and medicine. The outstanding properties of nanomaterials set them apart from traditional materials. It is expected that they will reach a key position in the aforementioned areas thus requiring assessement and examination of their potential for adverse health effects [1-4].

In fact, the World Health Organization has already reported more than 2 million premature deaths associated

with particulate matter air pollution each year [5]. Consequently, airborne nanoparticles, which are commonly categorized as fine particles with a thermodynamic diameter $0.1\mu m < d_p < 1\mu m$ and ultrafine particles with a thermodynamic diameter $d_p < 0.1\mu m$, have been the subject of several recent toxicological and epidemiological studies. These have reported an association between the increased exposure to airborne fine and ultrafine particles and adverse health effects, ranging from increased hospitalizations for treatment of respiratory diseases to increased risk of lung cancer [6, 7].

Apart from several effects such as the toxicity of the particle and the particle processing and translocation to secondary organs, the particle deposition and clearance have significant health implications [8]. The deposition is therefore the main subject of this study. The key factors influencing the total nano-sized particle deposition and the location of deposition hot-spots are the particle size, the inhalation and exhalation flow rate and the morphology of the human lung.

Reports of in vitro and in vivo ultrafine particle deposition measurements in the human lung are still rare. This is mainly due to the difficulties in the generation of ultrafine particles, the detection of their number concentration and the visualization of their distribution within the lung.

On the other hand, Computational Fluid Dynamics (CFD) has already shown its potential to complement experimental studies by predicting the air flow as well as the motion and deposition of nanoparticles in the human airways [9]. Applications range from simulations in simplified and realistic upper airway models [10-12] and simplified models of the tracheo-bronchial tree with multiple bifurcations [13, 14] to complex nasal-oral-tracheobronchial models [15]. However, the major weakness of the published numerical studies is the lack of a complete validation of the results by comparing them to experimental flow field and deposition measurements in the same model.

For this reason, the goal of the present study is to simulate and subsequently validate numerical results of the laminar-turbulent flow field and the total and local deposition of ultrafine particles in a human upper airway model, which shows all relevant morphological features of a realistic computer-tomography based model.

To numerically study the macroscopic motion of ultrafine particles, it is common practice to use the so-called Eulerian mass transport model. As the nanoparticle volume fraction of ambient particulate matter is very small, this model assumes that the particle state only depends on the state of the flow field and that their momentum exchange has an negligible effect on the flow. Consequently, the particles are treated as a one-way-coupled passive scalar, which also agrees with the widely accepted classification map for particle-laden turbulent flows proposed in [16]. The major advantage of this method over discrete methods, where a momentum equation has to be solved for every single particle, is its' applicability to a very large number of
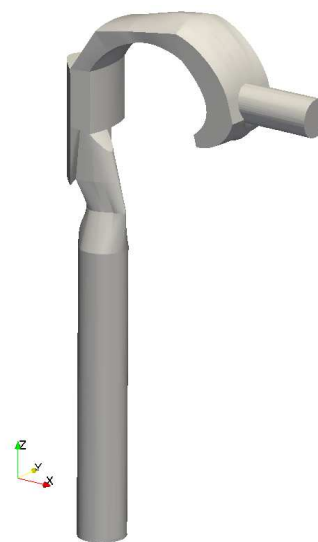
Figure 1 Isometric view of the upper airway model (UAM) geometry.

particles at very low computational cost.

Experimental Method

The conducted experiments aim to generate monodisperse ultrafine particles of different thermodynamic diameter and to measure their deposition in a cast of the human upper airway model under three different physiologically relevant inspiratory flow rates. The 3D geometry of the upper airway model, which is depicted in Figure 1, and the corresponding silicone cast are retrieved from previous work [17, 18].

Nano-sized Carbon particles are generated by spark ignition using a Carbon electrode in an Argon gas stream (GFG 100, Palas, Karlsruhe, Germany). During ignition, small amounts of carbon evaporate on the surface of the electrode and subsequently condense to form primary chain-like nanoparticles. A transmission elelectron miscroscopy (TEM) image of sample nanoparticles after their generation is given in Figure 2. Directly behind the outlet of the spark generation chamber, the highly charged particles are quasi-neutralized to Boltzmann equilibrium by using a Kr-85 source. In order to avoid further coagulation, the aerosol is diluted with air. A similar procedure had previously been carried out to generate Titanium Dioxide nanoparticles [19].

After the aerosol generation, the high initial particle concentration is significantly reduced by inserting a filter downstream of the spark generation chamber.

Monodisperse particle fractions with a geometric standard deviation $gsd < 1.15$ are then extracted using a Differential Mobility Analyser (DMA, Model 3071A, TSI Inc., Aachen Germany) and their charge level is again reduced using a Am-241 source. The concentration of the extracted monodisperse aerosol is always smaller than $10^4 \frac{p}{cm^3}$.

In order to change the size distribution and the thermodynamic particle diameter of the monodisperse particle
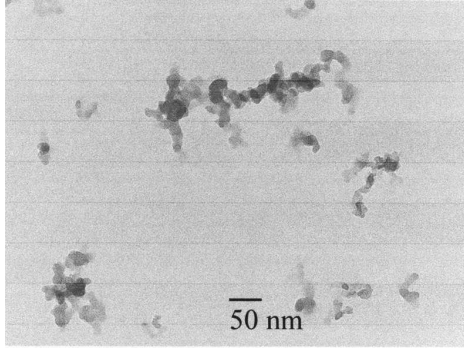
Figure 2 TEM image of sample chain-like nanoparticle agger-agtes after generation [19]

fraction respectively, the ignition frequency and the electrical deflection field (voltage) is varied. A higher ignition frequency results in a higher particle concentration and subsequent coagulation, so that larger particles are formed. Accordingly, higher deflection voltages of the DMA allow larger particles to pass the device. Overall, particles of four different thermodynamic diameters $d_p = 14.5, 20, 32$ and $52 nm$ are generated. The particle size distribution of the monodisperse aerosol is measured with a scanning mobility particle sizing system (SMPS, DMA model 3071 and CPC model 3022, both TSI Inc., Aachen, Germany) as shown in Figure 3.

Three different physiologically relevant steady volume flow rates of $Q_1 = 10 \frac{l}{min}$, $Q_2 = 20 \frac{l}{min}$ and $Q_3 = 30 \frac{l}{min}$ are generated using a pump which is connected to the outlet downstream of the cast of the upper airway model.

Particle number concentrations are calculated at two different measurement points, directly in front of the inlet of the upper airway cast (point #1) and directly behind the outlet of the cast (point #2) using a Concentration Particle Counter (CPC, Model 3010 TSI Inc., Aachen, Germany). The deposition fraction is calculated based on the detected particle concentration C as

$$DF = \frac{C_{\#1} - C_{\#2}}{C_{\#1}} \,, \tag{1}$$

where the subscripts denote the corresponding measurement point, either in front of the cast inlet or behind the cast outlet. A sketch of the experimental setup is shown in Figure 3.

Numerical Method

The governing equations describing incompressible fluid flow are the equation of continuity (1) and the Navier-Stokes equations (2). Using Einstein's summation convention for the indexing of the spatial direction (x, y, z) and the velocity vector components (u, v, w), they can be written as

$$\frac{\partial u_i}{\partial x_i} = 0, \tag{2}$$

$$u_j \frac{\partial u_i}{\partial x_j} = -\frac{1}{\rho} \frac{\partial p}{\partial x_i} + \frac{\partial \tau_{i,j}}{\partial x_j} \,, \tag{3}$$
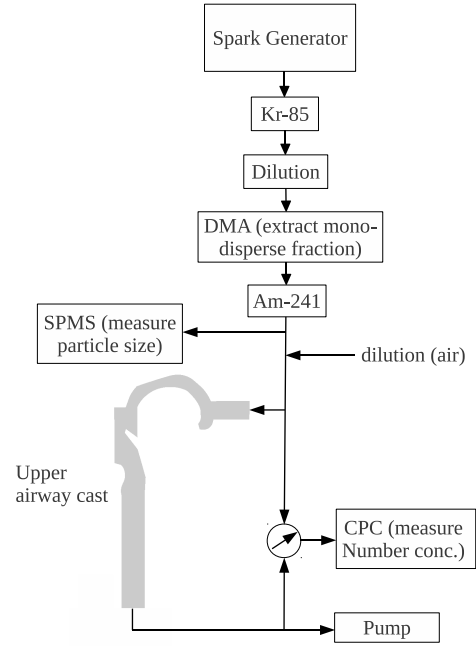
Figure 3 Schematic of the nano-sized carbon particle generation and particle size and concentration measurement.

with $\tau_{i,j}$ denoting the stress tensor. Performing Reynolds averaging on the governing equations and following Reynolds conditions yields the Reynolds-averaged Navier-Stokes (RANS) equations

$$\frac{\partial \overline{u}_i}{\partial x_i} = 0 \,, \tag{4}$$

$$\overline{u}_j \frac{\partial \overline{u}_i}{\partial x_j} = -\frac{1}{\rho} \frac{\partial \overline{p}}{\partial x_i} + \frac{\partial}{\partial x_j} \left(\overline{\tau}_{i,j} - \overline{u'_i u'_j} \right) \,, \tag{5}$$

with $-\overline{u'_i u'_j}$ denoting the specific Reynolds stress tensor. Following the Boussinesq approximation, the specific Reynolds stress tensor is modeled as

$$-\overline{u'_i u'_j} = \nu_t \left(\frac{\partial \overline{u}_i}{\partial x_j} + \frac{\partial \overline{u}_j}{\partial x_i} \right) - \frac{2}{3} k \delta_{i,j} \,, \tag{6}$$

with ν_t denoting the turbulent kinematic viscosity.

The turbulent kinematic viscosity ν_t is calculated using the k-ω SST RANS model [21]. It is based on the solution of a transport equations for the turbulent kinetic energy k and the specific dissipation rate ω. The key idea which sets the model apart from the traditional k-ω RANS model is a blend to switch between the k-ω RANS model in the near wall region and the k-ε RANS model in in the core region of the flow. More details on the definition of the blending function as well as of model constants can be found in [21]. It should be noted, that the model is used in its standard high-Reynolds version, thus leaving out low-Reynolds correction terms.

Since the particles are modeled as a one-way-coupled passive scalar, their motion is described by solving an advection-diffusion equation (7) for the particle concen-

tration C. It can be written as

$$u_j \frac{\partial C}{\partial x_j} = \frac{\partial}{\partial x_j} \left(D \frac{\partial C}{\partial x_j} \right) , \qquad (7)$$

with D denoting the diffusion coefficient of the particles. It is calculated as proposed in [22] by

$$D = \frac{k_b T C_s}{3\pi\mu d_p} , \qquad (8)$$

with k_b denoting the Boltzmann constant, T the temperature, μ the dynamic viscosity, d_p the thermodynamic particle diameter and C_s the Cunningham slip correction factor calculated as proposed in [23] by

$$C_s = 1 + Kn \left(1.142 + 0.558 \, e^{-\frac{0.999}{Kn}} \right) . \qquad (9)$$

Here, Kn denotes the Knudsen number. Performing Reynolds averaging and following Reynolds conditions on equation (7) yields

$$\overline{u}_j \frac{\partial \overline{C}}{\partial x_j} = D \frac{\partial \overline{C}}{\partial x_j} - \frac{\partial \overline{u_i' C'}}{\partial x_j} . \qquad (10)$$

The closure of the scalar-flux term $-\overline{u_i' C'}$ is accomplished by using a gradient-diffusion hypothesis, so that

$$-\overline{u_i' C'} = D_t \frac{\partial \overline{C}}{\partial x_j} . \qquad (11)$$

Here, D_t denotes the turbulent mass diffusion coefficient, which is modelled as

$$D_t = \frac{\nu_t}{Sc_t} . \qquad (12)$$

The turbulent Schmidt number Sc_t is treated as a global parameter and set to $Sc_t = 0.9$ [11, 24].

At the wall (subscript w), no-slip boundary conditions are applied for the velocity as well as for the turbulent kinetic energy, so that $u_{w,i} = 0$ and $k_w = 0$. Furthermore, the wall is assumed to be perfectly absorbing the ultrafine particle, so that $C_w = 0$. The specific dissipation rate in the viscous sublayer is calculated according to [21] as

$$\omega_{w,j} = \frac{6\,\nu}{0.075\, y_{0,j}^2} , \qquad (13)$$

where $y_{0,j}$ denotes the distance between the center of a wall face f_j and the center of the closest cell c_j normal to f_j. For the pressure p_w, zero-gradient boundary condition are applied at the wall.

The inlet profiles of all flow quantities are assumed to be block profiles. The inlet velocity u_{in} is set according to the considered inlet mass flow rate, while the initial inlet value of the turbulent kinetic energy k is calculated as

$$k_{in} = \frac{3}{2} \left(I_{in}\, u_{in} \right)^2 , \qquad (14)$$

where I_{in} denotes the core turbulence intensity of a fully developed turbulent pipe flow. The intensity at the inlet is calculated as

$$I_{in} = 0.16 Re_{in}^{(-0.125)} , \qquad (15)$$

with Re_{in} denoting the Reynolds number based on the inlet diameter and the inlet velocity. The initial value of the specific dissipation rate is calculated as

$$\omega_{in} = C_\mu^{(-0.25)} \frac{\sqrt{k}}{l_t} , \qquad (16)$$

where C_μ is a constant set to $C_\mu = 0.9$ and l_t the turbulence length scale in a fully developed turbulent pipe flow. It is calculated as

$$l_t = 0.07\, d_{in} . \qquad (17)$$

The amount of particles depositing on the wall is quantified by the deposition fraction (DF). In the framework of the Eulerian mass transport model, it is calculated as

$$DF = \frac{\dot{m}_w}{\dot{m}_{in}} , \qquad (18)$$

where the mass flow rate at the inlet $\dot{m}_{in}$ and the mass flow rate to the wall $\dot{m}_w$ are computed as

$$\dot{m}_{in} = \rho_m u_{in} 2\pi r_{in} , \qquad (19)$$

$$\dot{m}_w = \sum_{j=1}^{N_w} \left(-\rho_m A_j \left(D + \frac{\nu_t}{Sc_t} \right) \frac{\partial \overline{C}}{\partial n} \right). \qquad (20)$$

Here, ρ_m denotes the air-nanoparticle mixture density defined as

$$\rho_m = \alpha_p \rho_p + (1 - \alpha_f)\, \rho_f , \qquad (21)$$

where the subscripts p and f stand for the particle phase and the fluid phase respectively and α for the phase volume fraction. Further, N_w denotes the number of wall faces and A_j the surface area of f_j. The local particle deposition is quantified by the deposition enhancement factor (DEF) as proposed in [25] by

$$DEF_j = \frac{\dot{m}_{w,j}/A_j}{\dot{m}_w/A} , \qquad (22)$$

where A is the total wall surface area. The deposition enhancement factor (22) is commonly employed for the identification of local deposition hot-spots [9-15, 26].

The governing equations are discretized and solved using the open-source CFD software package OpenFOAM® [27, 28]. It uses the finite-volume method on three-dimensional arbitrarily unstructured meshes. Details on the discretisation procedure of the gradient, divergence and Laplace operator can be found in [29].

The laminar-turbulent flow field is computed using the already existing solver *simpleFoam*, a steady-state solver for incompressible, turbulent flows, which uses

the SIMPLE (Semi-Implicit Method for Pressure-Linked Equations) algorithm [30] for the pressure-velocity coupling.

The particle motion and equation (10), (11) and (12) in particular are computed using the *turbMassDiffusionFoam* solver. It is an extension of the already existing solver *scalarTransportFoam*. It is extended by equation (12), so that the *turbMassDiffusionFoam* solver accounts for the effect of turbulence on the particle motion. Similar to the *simpleFoam* solver, it is a steady-state solver, which uses under-relaxation of the flow variables to iterate the solution until convergence.

The procedure to obtain the flow field and the resulting particle motion and deposition for a specific inlet volume flow rate and particle diameter is as follows:

1. Use *simpleFoam* to solve the flow equations until convergence and write out the velocity field and the turbulent kinematic viscosity field.

2. Use these fields as the initial field condition in the *turbMassDiffusionFoam* solver. If different computational grids are used, the fields are mapped and interpolated onto the new grid.

3. Solve the particle equation until convergence using the *turbMassDiffusionFoam* solver and write out the particle concentration field.

4. Calculate the total deposition fraction DF and the deposition enhancement DEF factor using the postprocessing utilities *depositionFraction* and *depositionEnhancementFactor*, which are developed for this purpose

According to the conclusions of recently performed mesh style studies [31, 32], the geometry is subdivided into multiple blocks and a purely hexahedral grid is generated using the commercial meshing software ANSYS® ICEM CFD™[33]. As can be seen in Figure 4a and 5b, blocks with a circle-like cross-section are meshed with an O-grid.

In order to accurately capture the near-wall flow field and the expected flow features, such as the forced flow seperation at the Epiglottis, the first grid point normal to the wall is systematically placed at a dimensionless wall distance $y^+ \leq 1$. In fact, the specific dissipation rate boundary conditions as proposed in [21] is only valid in the viscous sub-layer. By using edge grading, the near-wall region is resolved while keeping the overall cell count as low as possible.

According to the experiments, simulations are performed for three different inlet volume flow rates $Q_1 = 10\frac{l}{min}$, $Q_2 = 20\frac{l}{min}$ and $Q_3 = 30\frac{l}{min}$. They correspond to the inlet Reynolds numbers $Re_1 = 615$, $Re_2 = 1230$ and $Re_3 = 2468$ based on the inlet velocity u_{in} and the inlet diameter d_{in}. As the flow with the highest inlet flow rate and Reynolds number respectively requires the finest near-wall grid discretization, the grid yielding grid-converged results for the case with $Q_3 = 30\frac{l}{min}$ and $Re_3 = 2468$
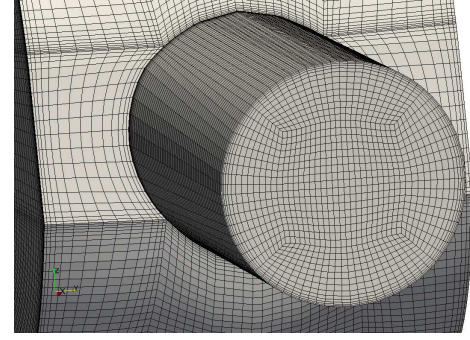
(a)
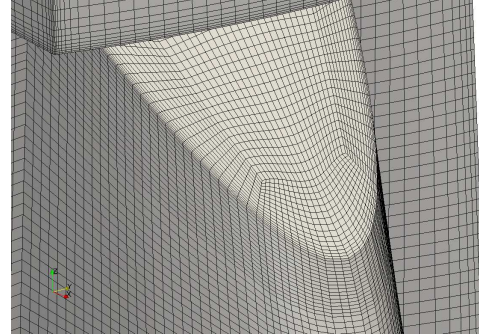
(b)

Figure 4 Illustration of the O-grid structure at circle-like cross-section of the inlet (a) as well as the Larynx and Trachea (b).

will be used for all fluid flow simulations.

Additionally to the four generated particle diameters, the deposition of even smaller particles with thermodynamic diameters of $d_p = 1$, 2, 5 and $10nm$ are studied in order to investigate an effect of the particle diameter on the deposition fraction.

Numerical Results and Discussion

Numerical results of velocity and turbulent kinetic energy for the flow with an inlet volume flow rate of $Q_3 = 30\frac{l}{min}$ are compared to available particle image velocimetry (PIV) and large-eddy simulation (LES) results [34] in four different section of the same upper airway model: $5mm$ above the Epiglottis (section E) and 1, 2 and 3 tracheal diameter downstream of the Larynx (section T1, T2 and T3). The approximate location of the four sections are depicted in Figure 7a. The profiles of the velocity magnitude and the turbulent kinetic energy measured in the four sections are displayed in Figure 5 and Figure 6.

Comparing all velocity profiles in section E against each other, it is apparent that neither the reference LES results nor the present k-ω SST RANS results are able to accurately capture the complex velocity profile predicted by the reference PIV measurements. Nevertheless, the main flow features are captured by both the reference LES and the present RANS results. Furthermore, the simulations correctly predict the typical velocity profiles downstream of the Larynx with the distinct velocity peak at $0.5 \leq x/D \leq 1$ refering to the high-velocity laryngeal jet.
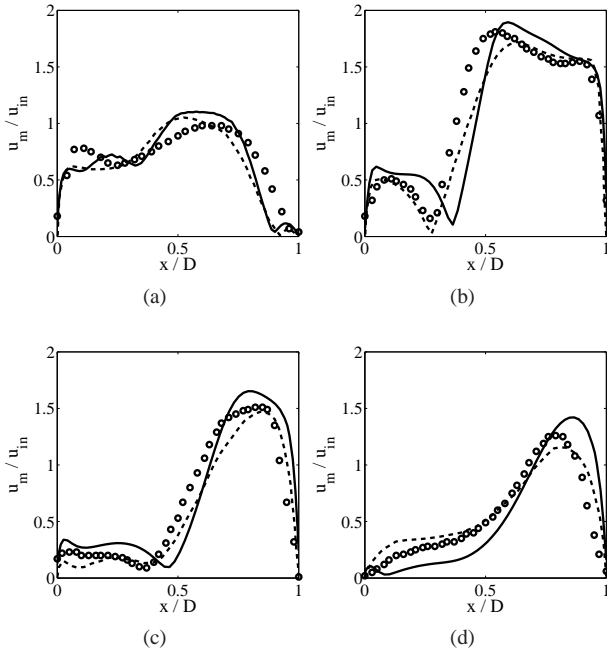
Figure 5 Profiles of two-component (u_x and u_z) velocity magnitude u_m normalized by the inlet velocity u_{in} in sections E (a), T1 (b), T2 (c) and T3 (d). ○ : experimental results [34], −− : LES results [34], − : present RANS results using the k-ω SST RANS model.
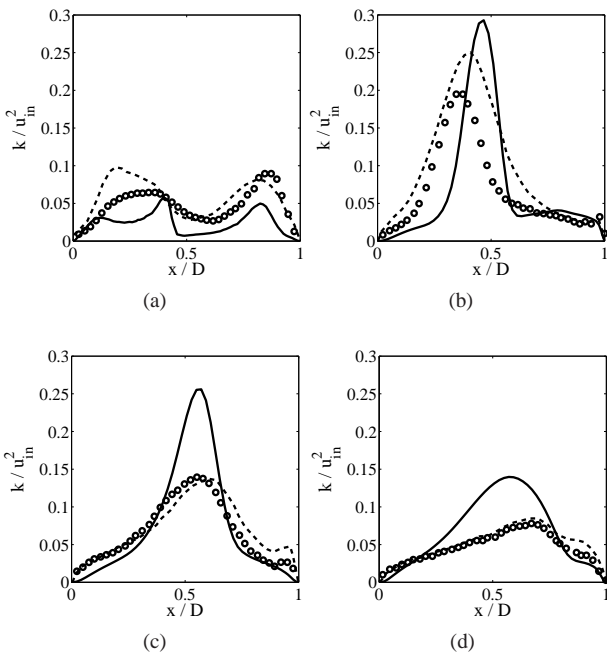
Figure 6 Profiles of turbulent kinetic energy k normalized by the square of the inlet velocity u_{in} in sections E (a), T1 (b), T2 (c) and T3 (d). ○ : experimental results [34], −− : LES results [34], − : present RANS results using the k-ω SST RANS model.
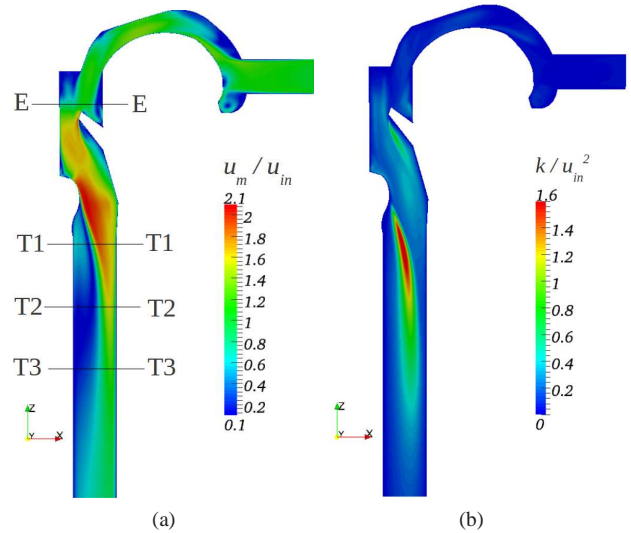
Figure 7 Two component (u_x and u_z) velocity magnitude u_m normalized by the inlet velocity (a) and turbulent kinetic energy k normalized by the square of the inlet velocity (b) in the central saggital plane.

However, it is observed in the corresponding section T1, T2 and T3 that the RANS simulation systematically overestimate the peak velocity, while the reference LES results show a good agreement with the experimental measurements in these particular regions. The overprediction of the laryngeal jet's peak velocity might be attributed to the missing low-Reynolds correction terms of the employed RANS turbulence model. These correction terms account for the viscous damping in the near-wall region. Considering the overall performance of the used RANS model, it can be stated that the predicted results are in acceptable agreement with the reference LES and experimental results.

The profiles of turbulent kinetic energy presented in Figure 6 support the oberservations made for the velocity profiles. Although the location of the peak turbulent kinetic energy is predicted correctly in the three sections downstream of the Larynx, its value is significantly overestimated. This again might be attributed to the missing low-Reynolds correction terms. As for the the velocity profiles, the LES results are in quite good agreement with the corresponding PIV measurements.

Contours of the two component velocity magnitude and the turbulent kinetic energy in a central saggital plane are shown in Figure 7a and 7b. Both contour plots show the relevant flow structures, i.e. the complex flow structure upstream of the Epiglottis, the laryngeal jet and the recirculation zone downstream of the Larynx constriction. Comparison with contour plots produced by PIV measurements [17] shows a quite good agreement of the flow field and the turbulent kinetic energy.

The suitability of the computational grid is investigated by calculating the dimensionless wall distance y_j^+ for each wall face. According to [21], the proposed bound-

(a) (b)
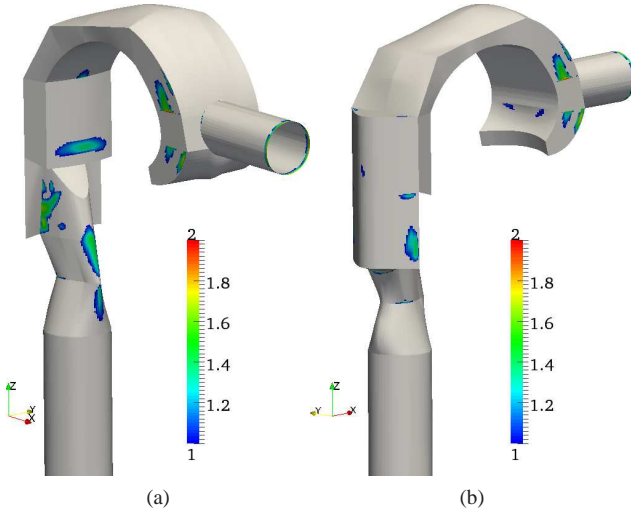
Figure 8 Contour plot of dimensionless wall distance y^+ in the range $1 \leq y^+ \leq 2$ for an inlet flow rate of $Q_3 = 30 \frac{l}{min}$.

ary conditions for ω (13) is valid, if $y^+ < 2$. Further, for a wall-resolving grid, the value of y^+ of the first grid-point normal to the wall should be $y^+ \approx 1$. Figure 8 shows the contours of y^+ in the range $1 < y^+ < 2$. It is apparent, that the dimensionless wall distance is sufficiently small at the entire wall surface.

The total particle deposition fraction DF is compared to the present experimental results for all flow rates and particles with a thermodynamic diameter of $d_p = 14.5, 20, 32$ and $52 nm$. Furthermore, comparison is made with numerical deposition results in two different simplified models of the human upper airways [10,11] and experimental in Vitro results [35, 36]. The percentage deposition fraction as a function of the particle diameter for $Q_1 = 10 \frac{l}{min}$, $Q_2 = 20 \frac{l}{min}$ and $Q_3 = 30 \frac{l}{min}$ is presented in Figure 9. Additionally the numerical as well as the experimental total deposition fraction results of the present study are summarized in Table 2.

The results displayed in Figure 9 clearly show two trends, which are already reported [9]. First, the deposition fraction is decreasing with an increasing particle diameter and second, the deposition fraction is decreasing with an increasing inhalation volume fow rate. In fact, against the background that the diffusion coefficient is decreasing with an increasing particle diameter and that the particle residence time is decreasing with an increasing flow rate, both trends are expected. The influence of the morphology of the upper airway model on the deposition fraction becomes visible when comparing the deposition fraction for $d_p = 1 nm$ up to $d_p = 10 nm$ reported in [10, 11]. An absolute difference of up to 20% is observed for $d_p = 1 nm$. Furthermore, it can already be seen, that the amount of deposited ultrafine particles in the upper airways is very small for $d_p > 10 nm$. Considering, that the deposition data are generated using not only different geometries but also different numerical as well as experimental methods, they are

Table 1 Percentage deposition fraction $DF[\%]$ obtained by experiments and numerical simulation in the same human upper airway model as a function of the particle diameter d_p and percantage deviation between the present experimental and numerical total deposition fraction results for $Q_1 = 10 \frac{l}{min}$ (a), $Q_2 = 20 \frac{l}{min}$ (b) and $Q_3 = 30 \frac{l}{min}$ (c).

(a)

$d_p[nm]$	14.5	20	32	52
$DF_{exp.}[\%]$	4.59	3.00	3.17	2.12
$DF_{num.}[\%]$	2.83	1.90	1.07	0.65
$\varepsilon[\%]$	38.34	36.67	66.25	69.34

(b)

$d_p[nm]$	14.5	20	32	52
$DF_{exp.}[\%]$	4.11	2.07	1.56	1.31
$DF_{num.}[\%]$	2.07	1.38	0.78	0.48
$\varepsilon[\%]$	49.64	33.33	50.00	63.36

(c)

$d_p[nm]$	14.5	20	32	52
$DF_{exp.}[\%]$	3.13	1.30	1.05	0.77
$DF_{num.}[\%]$	1.70	1.12	0.64	0.40
$\varepsilon[\%]$	45.67	13.85	39.05	48.05

in good quantitative agreement.

Comparing the achieved total deposition fraction data, it is apparent that there is still a significant discrepancy between numerical simulations and experiments. The percentage deviation ranges from $\varepsilon[\%] = 13.85$ for $d_p = 20 nm$ and $Q_3 = 30 \frac{l}{min}$ up to $\varepsilon[\%] = 69.34$ for $d_p = 52 nm$ and $Q_1 = 10 \frac{l}{min}$. However, the importance of a higher accuracy is questionable, as the overall amount of deposited ultrafine particles is very small.

Contour plots of the deposition enhancement factor (DEF) are presented in Figure 10 and 11 for the deposition of $d_p = 14.5 nm$ and $d_p = 52 nm$ particles at $Q_1 = 10 \frac{l}{min}$.

Although the overall deposition pattern is quite similar for both particle diameters, the DEF contours for $d_p = 10 nm$ shows more discrete deposition hot-spots with $DEF > 4$. This can be clearly seen at the undersite of the tongue and the pharyngeal wall, Figure 10, as well as at the epiglottal stop, Figure 11.

Conclusions and Outlook

The obtained flow field results for the volume flow rate $Q = 30 \frac{l}{min}$ are in acceptable agreement to the reference LES and experimental results. Nevertheless, it is observed that the peak velocity of the laryngeal jet is overestimated in sections T1, T2 and T3 and that the reference LES results match the experimental results condsiderably better. This behaviour is attributed to the missing low-Reynolds correction terms which account for viscous damping effects in the viscous sublayer. This effect is also observed for the profiles of turbulent kinetic energy. Although the peak location is correctly predicted, the peak value is overpredicted systematically downstream of the Larynx.

The achieved local and total deposition fraction results
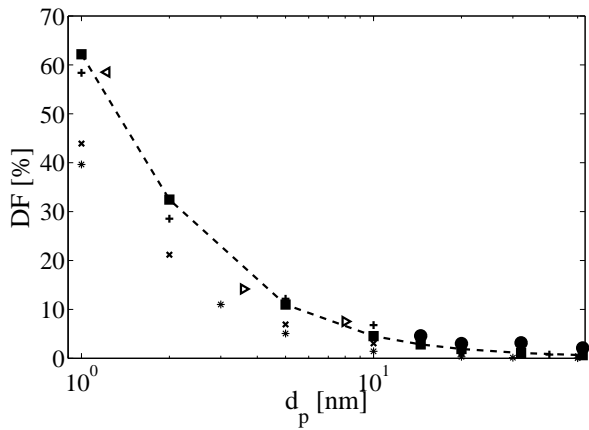
(a)
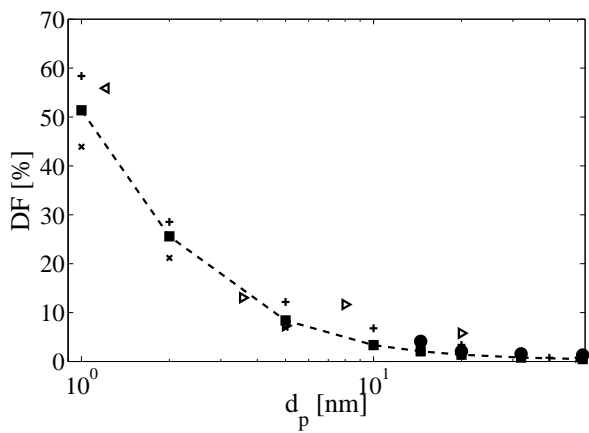
(b)
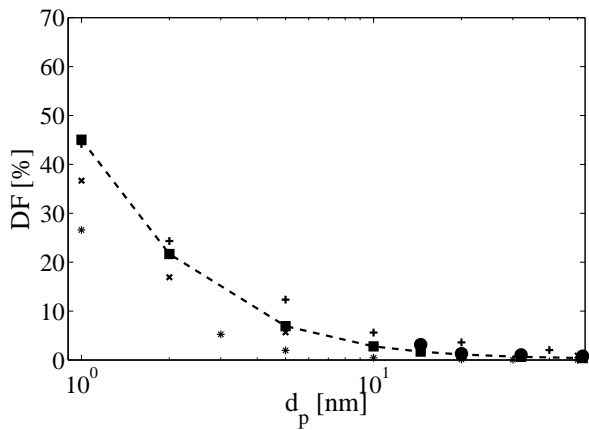
(c)

Figure 9 Total percentage deposition fraction $DF[\%]$ as a function of the particle diameter for $Q_1 = 10\frac{l}{min}$ (a), $Q_2 = 20\frac{l}{min}$ (b) and $Q_3 = 30\frac{l}{min}$ (c). x : Eulerian mass transport model [11], $+$: Euler-Lagrange method [11], $*$: Eulerian mass transport model [10], $\triangleleft$: experimental results [35], $\triangleright$: experimental results [36], $\bullet$: present experimental results, see Table 2 ,$-\blacksquare-$: present numerical results, see Table 2.
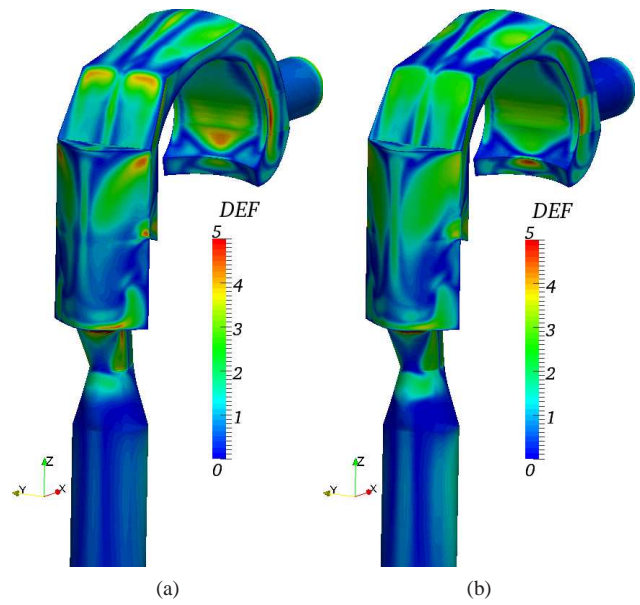
(a)   (b)

Figure 10 Isometric back view on contours of deposition enhancement factor DEF predicted at the Epiglottis and Larynx corresponding to the deposition of nanoparticles with a thermodynamic diameter $d_p = 14.5nm$ (a) and $d_p = 52nm$ (b) for a volume flow rate of $Q_1 = 10\frac{l}{min}$.
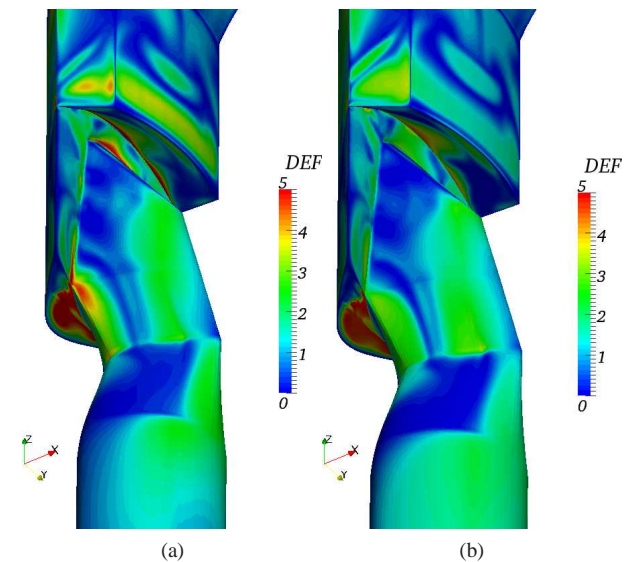
(a)   (b)

Figure 11 Contour of deposition enhancement factor (DEF) predicted at the Epiglottis and Larynx corresponding to the deposition of nanoparticles with a thermodynamic diameter $d_p = 14.5nm$ (a) and $d_p = 52nm$ (b) for a volume flow rate of $Q_1 = 10\frac{l}{min}$.

show the expected effects of the inhalation flow rate and the particle diameter on the amount of the deposited particles and the deposition pattern. Nonetheless, the comparison of experimental and numerical deposition fraction values shows a significant difference, which might be related to both the inaccurate prediction of the turbulent kinetic energy and the turbulent kinematic viscosity respectively and the near-wall concentration gradient. However, for small deposition fractions of $DF < 2\%$ as monitored for $d_p = 20nm$ it is questionable, if a more accurate prediction is necessary or if a statement of the approximate amount of deposited particles, i.e. $DF < 5\%$, is sufficient.

It is expected, that extending the k-ω SST RANS model with low-Reynolds corrections terms as proposed in [21] will significantly improve the near-wall as well as the overall flow field predictions. An even more advanced model is the recently proposed γ-Re_θ RANS model [37]. It extends the used k-ω SST model by a transport equation for the turbulence intermittency γ and for the momentum thickness Reynolds number Re_θ as an indication for the onset of transition. However, the computational cost will also increase with extending the turbulence model. Furthermore, previous studies have already shown that LES is superior to RANS for the accurate prediction of the complex mean flow field human upper airways [10, 33]. It allows not only the analysis of the time-averaged flow fields, but also of the large scale turbulent structures.

However, even if the flow field is computed using LES and accurate dynamic subgrid-scale models, the scalar-flux term is commonly modeled using the gradient diffusion hypothesis [10]. The major drawback of this hypothesis is the assumption of isotropic turbulence which is invalid for the laminar-turbulent flow in the human upper airways. Thus, a major accuracy improvement is expected by solving the fluid and particle equations in a coupled manner using LES and a localised dynamic subgrid-scale closure not only for the residual stress tensor but also for the scalar-flux term [38]. Although this method will be computationally expensive, it gives accurate instantaneous and time-averaged velocity and particle concentration profiles as well as insight in the dynamic interaction between the turbulent flow and the particle motion and local deposition.

There are several other ways to increase the realism of the model to mimic the real world inhalation and exhalation of airborne fine and ultrafine particles. They range from applying a physiologically realistic breathing pattern and consideration of a polydisperse aerosol to extending the upper airway model with a realistic model of the tracheo-bronchial tree with multiple generations.

Despite the huge potential of CFD for the simulation of the very complex flow in the human airways, their validation by means of experimental results will remain one of the major issues.

Acknowledgements

References

[1] M. Geiser, W. G. Kreyling, Deposition and biokinetics of inhaled nanoparticles, *Particle and Fibre Toxicology* **7**, pp. 1-17 (2010)

[2] W. G. Kreyling, M. Semmler-Behnke, W. Möller, Health implications of nanoparticles, *Journal of Nanoparticle Research* **8**, pp. 543-56 (2006)

[3] A. Ibald-Mulli, H.-E. Wichmann W. G. Kreyling, A. Peters, Epidemiological Evidence on Health Effects of Ultrafine Particles, *Journal of Aerosol Medicine* **15**, pp. 189-201 (2002)

[4] H. Schulz, V. Harder, A. Ibald-Mulli, A. Khandoga, W. König, F. Krombach, R. Radykewicz, A. Stampfl, B. Thorand, A. Peters, Cardiovascular Effects of Fine and Ultrafine Particles, *Journal of Aerosol Medicine* **18**, pp. 1-22 (2005)

[5] World Health Organization (WHO), Air quality guidelines. Global update 2005. Particulate matter, ozone, nitrogen dioxide and sulfur dioxide (2006)

[6] G. Oberdörster, Pulmonary effects of inhaled ultrafine particles, *International Archives of Occupational and Environmental Health* **74**, pp. 1-8 (2001)

[7] U. S. Akhtar, J. A. Scott, A. Chu, G. J. Evans, In vivo and In vitro Assessment of Particulate Matter Toxicology, *Environmental Science and Engineering* **74**, pp. 427-449 (2011)

[8] O. Schmid, W. Möller, M. Semmler-Behnke, G. A. Ferron, E. Karg, J. Lipka, H. Schulz, W. G. Kreyling and T. Stöger, Dosimetry and toxicology of inhaled ultrafine particles, *Biomarkers* **14**, pp. 67-73 (2009)

[9] C. Kleinstreuer and Z. Zhang, Airflow and Particle Transport in the Human Respiratory System, *Annu. Rev. Fluid Mech.* **42**, pp. 301-334 (2010)

[10] Z. Zhang and C. Kleinstreuer, Laminar-to-turbulent fluid-nanoparticle dynamics simulations: Model comparisons and nanoparticle-deposition applications, *International Journal of Numerical Methods in Biomedical Engineering* (2011)

[11] P. W. Longest and J. Xi, Effectiveness of Direct Lagrangian Tracking Models for Simulating Nanoparticle Deposition in the Upper Airways, *Aerosol Scince and Technology* **41**, pp. 380-397 (2007)

[12] Z. Zhang, C. Kleinstreuer, J. F. Donohue and C. S. Kim, Comparison of micro- and nano-size particle depositions in a human upper airway model, *Journal of Aerosol Science* **36**, pp. 211-233 (2005)

[13] A. Comerford, G. Bauer and W. A. Wall, Nanoparticle transport in a realistic model of the tracheo-bronchial region, *International Journal for Numerical Methods in Biomedical Engineering* **26**, pp. 904-914 (2010)

[14] Z. Zhang, C. Kleinstreuer and C. S. Kim, Airflow and Nanoparticle Deposition in a 16-Generation Tracheobronchial Airway Model, *Annals of Biomedical Engineering* **36**, pp. 2095-2110 (2008)

[15] Z. Zhang and C. Kleinstreuer, Computational analysis of airflow and nanoparticle deposition in a combined nasal-oral-tracheobronchial airway model, *Journal of Aerosol Science* **42**, pp. 174-194 (2011)

[16] S. Elgobashi, An updated Classification Map of Particle-Laden Turbulent Flows, *Fluid Mechanics and Its Applications* **81**, pp. 3-10 (2006)

[17] Mark Brouns, Numerical and experimental study of flows and deposition of aerosols in the upper human airways, PhD Thesis, Vrije Universiteit Brussel, Brussels, Belgium (2007)

[18] S. Verbanck, H. S. Kalsi, M. F. Biddiscombe, V. Agnihotri, B. Belkassem, C. Lacor and O. S. Usmani, Inspiratory and expiratory aerosol deposition in the upper airway, *Inhalation Toxicology* **23**, pp. 104-111 (2011)

[19] C. Roth, G. A. Ferron, E. Karg, B. Lentner, G. Schumann, S. Takenaka and J. Heyder, Generation of ultrafine particles by spark discharging, *Aerosol Science and Technology* **38**, pp. 228-235 (204)

[20] W. G. Kreyling, P. Biswas, M. E. Messing, N. Gibson, M. Geiser, A. Wenk, M. Sahu, K. Deppert, I. Cydzik, C. Wigge, M. Semmler-Behnke, Generation and characterization of stable, highly concentrated titanium dioxide nanoparticle aerosols for rodent inhalation studies , *Journal of Nanoparticle Research* **13**, pp. 511-524 (2011)

[21] F. Menter, J. Carregal Ferreira, T. Esch and B. Konno, The SST Turbulence Model with Improved Wall Treatment for Heat Transfer Predictions in Gas Turbines, In proceedings of the *International Gas Turbine Congress*, Tokyo, Japan (2003)

[22] W. H. Finlay, The Mechanics of Inhaled Pharmaceutical Aerosols: An Introduction, *Academic Press* (2001)

[23] M. D. Allen and O. G. Raabe, Slip correction measurements for aerosol particles of doublet and triangular triplet aggregates of spheres, *Journal of Aerosol Science* **16**, pp. 57-67 (1985)

[24] H. Shi, C. Kleinstreuer, Z. Zhang and C. S. Kim, Nanoparticle transport and deposition in bifurcating tubes with different inlet conditions, *Physics of Fluids* **16**, pp. 2199-2213 (2004)

[25] I. Balashazy, W. Hofmann, T. Heistracher, Computation of local enhancement factors for the quantification of particle deposition patterns in airway bifurcations, *Journal of Aerosol Science* **30**, pp. 185-203 (1999)

[26] I. Balashazy and W. A. Hofmann and T. Heistracher, Local particle deposition patterns may play a key role in the development of lung cancer, *Journal of Applied Physiology* **94**, pp. 1719-1725 (2003)

[27] OpenFOAM®, www.openfoam.com

[28] H. G. Weller, G. Tabor, H. Jasak, C. Fureby, A tensorial approach to computational continuum mechanics using object-oriented techniques, *Computers in Physics* **12**, pp. 620-631 (1998)

[29] H. Jasak, Error Analysis and Estimation for the finite Volume Method with Applications to Fluid Flows, PhD Thesis, Imperial College of Science, Technology and Medicine, London, United Kingdom (1996)

[30] J. H. Ferziger, M. Peric, Computational Methods for Fluid Dynamics, 3$^\text{rd}$ Edition, *Springer* (2001)

[31] P. W. Longest, S. Vinchurkar, Effects of mesh style and grid convergence on particle deposition in bifurcating airway models with comparisons to experimental data, *Medical Engineering & Physics* **29**, pp. 350-366 (2007)

[32] S. Vinchurkar, P. W. Longest, Evaluation of hexahedral, prismatic and hybrid mesh styles for simulating respiratory aerosol dynamics, *Computers & Fluids* **37**, pp. 317-331 (2008)

[33] ANSYS® ICEM CFD™, www.ansys.com

[34] S. T. Jayaraju, M. Brouns, C. Lacor, B. Belkassem and S. Verbanck, Large eddy and detached eddy simulations of fluid flow and particle deposition in a human mouth-throat, *Journal of Aerosol Science* **39**, pp. 862-875 (2008)

[35] Y. S. Cheng, Y. F. Su. H. C. Yeh and D. L. Swift, Deposition of Thoron Progeny in Human Head Airways, *Aersol Science and Technology* **18**, pp. 359-375 (1993)

[36] K. H. Cheng, Y. S. Cheng, H. C. Yeh and D. L. Swift, An Experimental Method for Measuring Aerosol Deposition Efficiency in the Human Oral Airway, *American Industrial Hygiene Association Journal* **58**, pp. 207-213 (1997)

[37] R. B. Langtry and F. R. Menter, Correlation-Based Transition Modeling for Unstructured Parallelized Computational Fluid Dynamics Codes, *AIAA Journal* **47**, pp. 2894-2906 (2009)

[38] W. Cabot and P. Moin, Large eddy simulation of sclar Transport with the dynamic subgrid-scale model, In *Large Eddy Simulation of Complex Engineering and Geophysical flows* (ed. B. Galperin and S. A. Orszag), Cambridge University Press, pp. 141-158 (1993)